Liquid water in cathode gas diffusion layers of PEM fuel cells:Identification of various pore filling regimes from pore network simulations

Pierre Carrere, Marc Prat

Liquid water in cathode gas diffusion layers of PEM fuel cells: Identification of various pore filling regimes from pore network simulations

P. Carrere, M. Prat *

Institut de Mécanique des Fluides de Toulouse (IMFT), Université de Toulouse, CNRS, Toulouse, France

A pore network model (PNM) aiming at simulating the liquid water pore filling in the cathode gas diffusion layer (GDL) in an operating PEM–fuel cell is presented. Compared to previous works, the model allows simulating a significantly larger range of operating regimes. It notably allows considering the situation where the channel gas is fully humidified both for low temperature operating conditions ($\sim$40 °C) and standard temperature operating conditions ($\sim$80 °C) as well as for intermediate operating temperatures. The model leads to results in good agreement with several experimental observations from the literature. This allows defining a regime diagram summarizing the main operating regimes identified in the course of the study, namely the dry regime, the dominant condensation regime, the dominant liquid injection regime, the mixed regime where both the capillarity controlled invasion in liquid phase from the adjacent layer and condensation are important. The proposed model opens up new perspectives for understanding the water transfer in proton exchange membrane fuel cells and the associated water management and performance degradation issues.

1. Introduction

Water management, i.e. [1], and degradation mechanisms [2,3] are two related major issues for the development of PEM-FC (Polymer Electrolyte Membrane Fuel Cell) technology. In this context, a better understanding of the water formation and transfer mechanisms within the fuel cell can be highly helpful. Surprisingly, in spite of the considerable worldwide research effort on this technology, these mechanisms are not yet fully understood. This constitutes an obstacle for the design of efficient and durable fuel cells whose improvements still largely rely on costly trial and error tests. As in other technological branches, numerical simulations can be expected to help reduce the number of tests and to serve as design tool but this, of course, implies that the key mechanisms are well modelled. In this context, the present paper is an attempt to clarify the mechanisms leading to the occurrence of liquid water in the cathode gas diffusion layer (GDL) from numerical simulations. As pointed out for instance in [4], GDLs are integral part of PEM-FCs and play a key role for the distribution of the reactant from the channel to the catalyst layer (CL) as well as for removing the water produced in the CL. Due to its significance, the water

issue in GDLs has been the subject of many experimental and numerical studies. On the experimental side, several groups have contributed to this field using X-ray tomography microscopy, e.g. [5–8], or neutron radiography, e.g. [9,10], techniques. These techniques allow obtaining information on the liquid water distribution within the GDL under PEMFC actual operation conditions. However, owing to spatial resolution problem, it is difficult to get information on the water in the adjacent CL or microporous layer (MPL). As a result, although highly interesting, the information obtained from these techniques is generally not sufficient to really understand the mechanisms at play. In this respect, the modelling works and the associated numerical simulations can be considered as complementary since they imply to make assumptions on the water formation and transfer mechanisms. This has motivated quite a few studies using various techniques, such as Lattice Boltzmann Method, e.g. [11], or pore network models (PNM) [12–29]. More classical continuum approaches based on the standard two-phase flow model for porous media have been also used, e.g. [30]. However, the lack of length scale separation characterizing the GDLs leads to question the relevance of the classical continuum approach to porous media in the case of GDLs, i.e. [31,32]. Combined with the fact that PNM computations are quite faster than LBM and easy to develop, this has led to the situation that PNM is nowadays the most popular numerical technique to study the

invasion of GDLs by liquid water. The present paper is also based on PNM. In this respect, the major objective of the paper is to propose an improved and more versatile PNM simulation tool compared to previous works. This means that the new PNM should be able to simulate a quite larger range of operating conditions than previous models. This new PNM will be validated by comparison with experimental data from the literature.

Actually, one can distinguish two main groups as regards the PNMs aiming at simulating the pore filling of the GDL by liquid water under in-situ conditions. The first group is by far the largest in number of articles, e.g. [12–23]. The main assumption for this group is that water enters the GDL in liquid phase from the CL or MPL /GDL interface. For this reason, the models of this group are referred to as Liquid Injection Pore Network Models (LIPNM). Also, the temperature of the GDL is implicitly assumed as spatially uniform and phase change phenomena are neglected. Related to this group, one can also mention the PNM presented in [24] where the water also enters the GDL in liquid form but with, in addition, the consideration of the evaporation phenomenon. The models of the second group [25–28], have been proposed much more recently. Compared to the models of the first group, a major difference is that liquid water can form within the GDL as a result of vapour condensation. Also, the temperature variations within the GDL are taken into account. This is actually a key feature in those models. Contrary to the models of the first groups, the assumption is made that water enters the GDL from the CL or the MPL in vapour phase and not in liquid phase. The development of the condensation PNM (CPNM) was motivated by the fact that experimental works, i.e. [9,10], show situations where the liquid water is confined under the ribs with no liquid water in the regions of the GDL below the channels. As discussed and shown in [26,27], the condensation PNM leads to results in fairly good agreement with those experiments. Owing to the crucial role of condensation, the PNMs of the first group should lead to very poor results in this case. This will be illustrated in the present article. The corresponding conditions were a standard operating temperature of 80 °C and possibly a high relative humidity in the channel. However, the condition of a fully humidified gas in the channel was not considered in the simulations presented in [26,27]. Interestingly, the visualisations of the water distribution obtained by X-ray tomography presented in [6] for a temperature of 80 °C but fully humidified channel gas conditions show liquid water distributions markedly different with liquid water present not only below the rib but also in the regions of the GDL below the channel. At lower temperatures, i.e. $T \approx 40$ °C, the liquid water distributions obtained by X-ray tomography also show that the liquid water can be present almost everywhere, both below the ribs and below the channels. In addition, the water distributions presented in [7] for the intermediate temperature of 60 °C indicate a strong influence of the relative humidity in the feed channels with liquid water again almost everywhere in the GDL when the gas in the channels is fully humidified.

In brief, as regards the PNMs, the situation is the following. The PNMs of the first group have never been compared to experimental results obtained by X-ray tomography or neutron radiography. They are unable to lead to consistent results with the experiments at $T = 80$ °C discussed in [26]. In this respect, the PNMs of the second group are much more satisfactory. However, tests with the PNMs of the second group do not lead to satisfactory results for the fully humidified channel gas conditions. Thus, there is a need for a PNM able to simulate properly all the cases mentioned above. Since the PNM of the second group lead to fairly good results at 80 °C when the relative humidity (RH) in the channel is less than 100%, the idea was to start from this type of model. We started from the one described in [26]. In addition to several improvements that will be indicated below, the main point is to consider

that water can enter the GDL both in vapour and liquid forms and not only in vapour form as in [26]. For this reason, this new PNM is called liquid-vapour Mixed Injection PNM (MIPNM). Here, it can be mentioned that such a mixed option as boundary condition at the GDL inlet was considered in the dynamic model presented in [29]. However, the heat transfer problem is not explicitly solved in this model and the simulations were performed in 2D only. No detailed comparisons with experimental results were presented. Although somewhat different and not exactly a PNM, the model presented in [33] can be also mentioned here since it seems that it combines both injection in liquid phase and condensation.

The paper is organized as follows. The new PNM is presented in Section 2. Section 3 is devoted to the calibration of an important parameter of the model. Section 4 proposes a comparison between experimental results and simulations from the three different PNMs, namely a PNM of the first group (LIPNM), a PNM from the second group (CPNM) and the new PNM (MIPNM). Section 5 is devoted to a short discussion. A diagram summarizing the main operating regimes identified in the course of the study is presented in Section 6. Conclusions are drawn in Section 7.

2. Liquid-vapour mixed injection pore network model

As mentioned previously, the liquid-vapour Mixed Injection Pore Network Model (MIPNM) is an extension of the condensation pore network model (CPNM) presented in [26] to simulate the water transfer in the cathode GDL of a fuel cell operating at standard operating temperature and reactant gas relative humidity below 100%. This model was based on the assumption that water enters the GDL in vapour phase. The major new feature here is to consider that the water produced in the CL can enter the GDL both in vapour and liquid phases. The same main phenomena in the cathode GDL as for the CPNM are considered with the MIPNM: namely water vapour transport, heat transfer, liquid-vapour phase change and liquid water transport.

2.1. GDL unit cell

As sketched in Fig. 1, simulations are performed over a domain referred to as the GDL unit cell. It corresponds to a section of the cathode GDL located under a central rib and two half channels. Unless otherwise mentioned, the rib width is $L_r = 960$ μm and the channel half-width is $L_{ch}/2 = 480$ μm. Spatially periodic boundary conditions are imposed along the lateral boundaries of the unit cell for each physical problem. The length of the computational domain in the y direction L_y (see Fig. 1) is less than its width $L_x = L_r + L_{ch}$. This allows reducing the computational time. After some tests, it was judged that L_y could be reduced to 800 μm without any noticeable impact on the liquid water distribution. Unless otherwise mentioned, the GDL thickness is $\delta_c = 200$ μm and the channel depth $H_{ch} = 480$ μm. Those values are representative of real GDLs. As in [26], the GDL in the unit cell is represented by a 3D regular cubic network of pores and throats. Pores and throats are referred to as the elements of the network. The network lattice spacing, which is the distance between two neighbour pores in the network, is $a = 40$ μm. This leads to represent the GDL unit cell by a $N_x \times N_y \times N_z$ pore network where N_x, N_y and N_z are the number of pores in the network in the in-plane transverse direction, the y direction and the through-plane direction respectively. Unless otherwise mentioned, $N_x = 48$, $N_y = 20$ and $N_z = 5$ pores.

The geometrical anisotropy of GDLs has been pointed out through several recent X-ray tomographic microscopy studies [34,35]. This anisotropy is expected to favour the liquid water invasion along through-plane oriented pathways. This anisotropy is
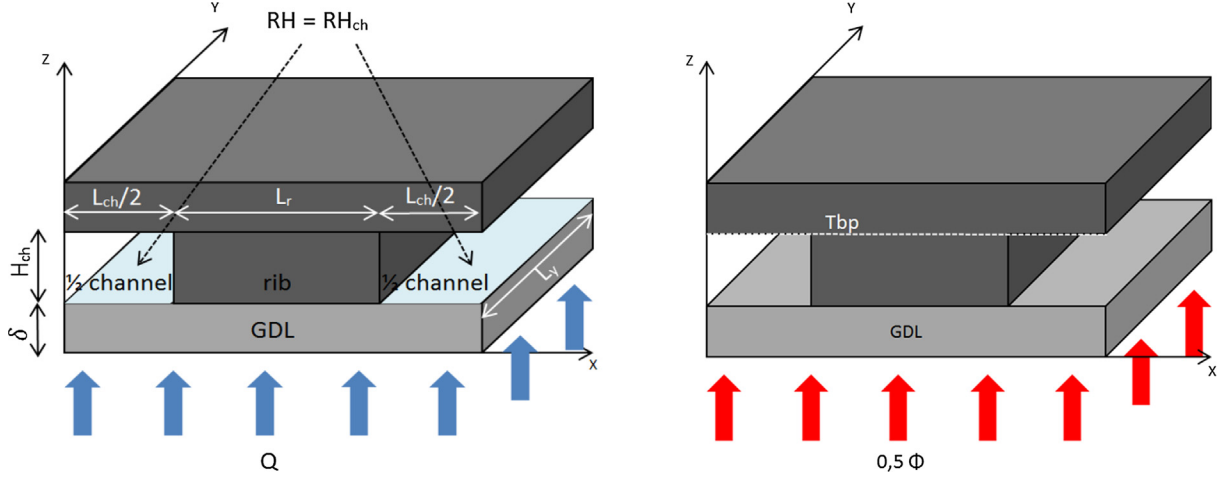
Fig. 1. Sketch of the GDL unit cell and schematics of water and heat transfer problems.

caused by the orientation of the carbon fibres during the roll-to-roll processing [36]. From X ray tomographic images, the anisotropy of GDL was recently characterized by a difference of shape between the in-plane and through-plane cross-section of the pores which are respectively elongated ellipses and circles [34]. For the simulations, the throat sizes are randomly chosen following uniform distribution laws between $d_{t\perp,min}$ and $d_{t\perp,max}$ for the throats in the through-plane direction and $d_{t//,min}$ and $d_{t//,max}$ for the throats in the in-plane directions. The values used for $d_{t\perp,min}$, $d_{t\perp,max}$, $d_{t//,min}$ and $d_{t//,max}$ are given in Table 1 These direction dependent distributions allow taking into account the GDL anisotropy properties.

Furthermore, the geometry is region dependent. Indeed, the mean pore size should decrease with the compression, e.g. [36]. This is in agreement with the work reported in [37] using X-ray computed tomography and reporting distinct distributions under the rib and under the channel. The compression of the rib leads to smaller pores. To take into account this compression effect under the rib, the throat sizes in the in-plane directions are reduced by a factor $\sqrt{\delta_c/\delta_{uc}}$ in the compressed region, i.e. below the rib, where $\delta_{uc} = 230$ μm is the thickness of the uncompressed GDL under the half channels and $\delta_c = 200$ μm is the thickness of the compressed GDL under the rib.

Finally, the pore sizes are adjusted so that the desired porosity $\varepsilon = 76\%$ of the GDL is imposed.

2.2. Transport problems to be solved

Although the various transport problems are solved using the PNM techniques, we present them for convenience in compact form using "macroscopic –like" equations. Details are available in previous publications, e.g. [26,27], and for this reason are not

repeated here. Actually, the PNM discretization of the various transport problems on the cubic network is quite similar to a finite volume discretization over a regular mesh, with a spatial step equal to the lattice spacing. In the standard PNM approach, i.e. [38], the local conductances vary from one throat to the other as the result of the throat and pore size spatial variability. As in [26], this local variability is not taken into account in what follows. Thus, it can be considered that we use a mean field approach in this respect. However, the variability between the region below the rib and the regions below the two half channels as well as the anisotropy of the microstructure is taken into account as explained below.

2.2.1. Vapour diffusion

For simplicity the gas phase is considered as a binary mixture of water vapour and air. Using Fick's law the problem to be solved regarding the vapour transport is expressed in compact form as:

$$\nabla \cdot (\boldsymbol{D}^* \cdot \nabla(cx_v)) = 0 \tag{1}$$

where $\boldsymbol{D}^*$ is the effective diffusion tensor of the vapour and $c = \frac{P_{ref}}{RT_{bp}}$ is the mole concentration of the gas phase defined at the bipolar plate temperature T_{bp}.

Due to the GDL anisotropy and the compression under the rib, the components of the effective diffusion tensor $\boldsymbol{D}^*$ are defined for every region and every direction: $D^*_{\perp c}$ for the compressed region in the through-plane direction, $D^*_{//c}$ for the compressed region in the in-plane directions, $D^*_{\perp uc}$ for the uncompressed region in the through-plane direction and $D^*_{//uc}$ for the uncompressed region in the in-plane directions. The values are presented in Table 1.

Table 1
Mass, heat and geometry parameters. D is the molecular diffusion of the water vapour. It depends on temperature and pressure ($D = 2.27 \times 10^{-5}$ m^2/s at $T = 80$ °C and $p_{tot} = 1.5$ bars).

	$\frac{D^*_{\perp uc}}{D}$ [−]	$\frac{D^*_{\perp c}}{D}$ [−]	$\frac{D^*_{//uc}}{D}$ [−]	$\frac{D^*_{//c}}{D}$ [−]
Effective diffusion coefficient [-]	0.25	0.25	0.7	0.5
	$\lambda_{\perp uc}$	$\lambda_{\perp c}$	$\lambda_{//uc}$	$\lambda_{//c}$
Thermal conductivity for dry GDL [W·m^{-1}·K^{-1}]	0.25	0.25	4.0	6.64
	$d_{t\perp,min}$	$d_{t\perp,max}$	$d_{t//,min}$	$d_{t//,max}$
Throat size distributions [μm]	14	22	10	18

At the GDL/channel interface, the water vapour molar fraction is imposed from the relative humidity of the gas flowing inside the channel (Fig. 1),

$$x_{v,ch} = \frac{RH_{ch}P_{vs}(T_{bp})}{P_{ref}} \tag{2}$$

where $P_{vs}(T_{bp})$ is the saturation vapour partial pressure at the bipolar plate temperature T_{bp} and RH_{ch} is the gas relative humidity. Both T_{bp} and RH_{ch} are inputs of the model. A zero flux condition is imposed at the GDL/rib interface.

Various boundary conditions can be applied at the GDL/CL interface since liquid, vapour or both vapour and liquid water injection conditions can be imposed. The corresponding boundary conditions are presented later. Whatever the boundary conditions at the GDL/CL interface, the total flux of water entering the GDL must be equal to:

$$Q = \beta \frac{i}{2F} \tag{3}$$

where β is a parameter introduced for taking into account that only a fraction of the produced water goes to the cathode side, i is the current density which is a model input and F is the Faraday's constant ($F = 96485.34$ C).

In every element of the network, pore or throat, that contains liquid water the local relative humidity is set to $RH = 100\%$, meaning that the liquid-vapour equilibrium is reached. Therefore, the molar fraction of water vapour in such an element is $x_v = P_{vs}(T)/P_{ref}$.

2.2.2. Heat transfer

The heat transfer problem is solved in both the bipolar plate (channel and rib) and the GDL to take into account the impact of the bipolar plate geometry on the temperature field. Thermal conduction with liquid-vapour phase change is considered,

$$\nabla \cdot (\lambda \cdot \nabla T) = S_{lv} \tag{4}$$

where λ is the local effective thermal conductivity tensor and S_{lv} is the source term associated with the phase change.

Like the effective diffusion coefficient, the thermal conductivity is different in the in-plane and the through-plane directions and in the compressed and uncompressed regions. At the scale of the discretization mesh associated with the pore network, thermal conductivities are effective parameters for the medium made of a mixture of carbon fibres and fluid in the pores. Since the GDLs are highly porous ($\varepsilon \sim 76\%$), the nature of the fluid phase can significantly impact the thermal conductivity because the thermal conductivity of liquid water (~ 0.61 W·m^{-1}·K^{-1}) is significantly larger than the one of air (~ 0.027 W·m^{-1}·K^{-1}). Compared to the thermal model developed in [26] an improvement made with the present model was to take into account the dependence of the local effective thermal conductivity on the local water saturation in the GDL. Based on the experimental results from [39], the following expression for the thermal conductivity was considered:

$$\lambda(S) = (\lambda_{saturated} - \lambda_{dry})S + \lambda_{dry} \tag{5}$$

This model assumes that the thermal conductivity linearly increases with the saturation S. The saturation S is the local volume fraction of the pore space occupied by liquid water. $S = 0$ in a dry region and $S = 1$ in a liquid fully saturated region. The values for $\lambda_{saturated}$ and λ_{dry} are adapted from experimental results presented in [39]. The experiments in [39] allow characterizing the through-plane thermal conductivity only. A similar functional dependence with the saturation, i.e. Eq. (6), was assumed in the in-plane direction. For the studied GDL, this leads to consider the following expression:

$$\lambda(S) = 0.42S + \lambda_{dry} \tag{6}$$

The various values of λ_{dry} for each direction and each region are presented in Table 1.

The consideration of the latent heat transfer associated with the liquid-vapour phase change is another noticeable improvement of the thermal model compared to the simplified version considered in [26]. The corresponding source term S_{lv} in Eq. (4) is non-zero only in pores containing liquid-gas interface. It is expressed as:

$$S_{lv} = h_{lv}\dot{m}_{net} \tag{7}$$

where h_{lv} (J/mol) is the water phase change enthalpy and $\dot{m}_{net}$ (mol/m^3/s) is the local net liquid-vapour phase change rate in the considered pore.

The heat Φ generated by the electrochemical reaction at the cathode CL is conducted through the GDL to the bipolar plates where the temperature T_{bp} is assumed constant. As sketched in Fig. 1, it is further assumed that only half of the generated heat is transferred on the cathode side:

$$0.5\ \Phi = 0.5\left(\frac{h_r}{2F} - U\right)i \tag{8}$$

where h_r is the reaction enthalpy ($h_r = 242000$ J·mol^{-1}) and U is the electrical tension which is deduced from a polarization curve adapted from [9].

2.2.3. Liquid water transport

The liquid water transport through the GDL is controlled by capillary forces. Since GDLs are generally treated with PTFE, the GDL is considered as hydrophobic. Assuming a good distribution of the PTFE all over the GDL, every element of the pore network is thus considered as hydrophobic. As a result and as in practically all the previous works using PNM for the study of GDLs, the liquid water displacement in the network follows the invasion percolation rules [40].

2.3. GDL liquid water filling algorithm

As mentioned previously, the crucial new feature compared to previous works, i.e. [26,27], lies in the consideration of evaporation and condensation processes in the GDL together with the possibility for the water to enter the GDL in both liquid and vapour phases. The corresponding liquid water invasion/filling algorithm can be summarized as follows (see also the flow chart of the algorithm in the appendix):

(1) The GDL is fully dried initially.
(2) All the produced water, as given by Eq. (3), is injected in vapour phase initially. The heat and mass problem are solved to obtain the temperature and water vapour molar fraction fields. This allows determining the relative humidity in every element of the network.
(3) A first nucleation step is performed. This step allows determining the elements in which condensation happens. Condensation occurs in an element of the network when the relative humidity in the element is such that $RH > \eta$ (with $\eta \geqslant 1$). Condensation happens step by step starting in the pore of maximum RH. Nucleation condensation consists in imposing an incipient liquid volume fraction (set to 1% in all the presented simulations) and a relative humidity $RH = 1$ in the considered element. After each nucleation – condensation step, the temperature and water vapour molar fraction fields are recomputed in the network so as to take into account the new distribution of liquid water. All the elements verifying the nucleation criterion $RH > \eta$ are identified again and this step is repeated until no new dry element verifies the nucleation criterion.

(4) At the end of the first nucleation step all the pores located in the first layer at the GDL/CL interface are checked. Among these pores, all of them where nucleation has occurred, if any, are identified. A fraction α of these pores becomes liquid injection points. The remaining fraction $(1 - \alpha)$ of these pores are considered as purely gaseous with a fixed relative humidity $RH = 100\%$. The reason for randomly choosing a number of liquid injection points can be seen as a way of taking into account the impact of the MPL, which is not explicitly modelled in the present effort. It is generally considered, e.g. [41,42], that the MPL contributes to prevent the GDL water flooding by selecting preferential water pathways. For this reason, we consider that liquid water enters the GDL through a finite number of injection points (this number is denoted by N_{inj}) and not all over the whole interface. It is important to note that the liquid injection points are specified during this step only. No new injection points are set during the next steps of the simulation despite the possible occurrence of new nucleation sites in the first layer at the GDL/CL interface during those steps. It would be interesting to develop a more refined algorithm to explore the significance of this issue. This is left for a future work.

At the end of step #4, three different kinds of boundary conditions are imposed in the pores located at the GDL inlet, corresponding to three different types of inlet pores. The pores where no nucleation was detected in step #3 are considered as gaseous. The water vapour molar flux Q given by Eq. (3) is imposed in those pores. They are shown in grey in Fig. 2. The pores where nucleation has occurred but which have not been selected in step #4 as liquid injection pores are considered as gaseous with a fixed relative humidity $RH = 100\%$. They are in blue in the example shown in Fig. 2. In such pores, the injected water flow rate is not imposed but is computed from the computation of the water vapour molar fractions in the network. The corresponding flow rate is denoted by Q_{comp}. The water liquid flow rate $Q_{liqwater}$ in each pore selected in step #4 as liquid injection point (in red in Fig. 2) is determined from the following mass balance assuming that the injection flow rate $Q_{liqwater}$ is the same in each liquid injection pore:

$$N_{inj}a^2 Q_{liqwater} = Qa^2 N_x N_y - \sum_{(i,j)gaseous\ RH<1} Qa^2 - \sum_{(i,j)gaseous\ RH=1} Q_{comp}a^2$$
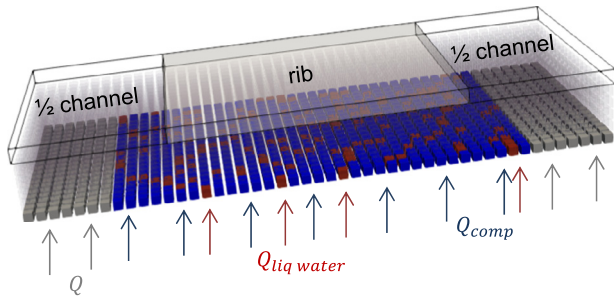
(9)

Fig. 2. Example of the first layer of GDL pores with the three types of pores at the inlet. Grey pores are gaseous with a relative humidity lower than 100%. The relative humidity is fixed at 100% in blue gaseous pores. Red pores are the chosen liquid injection pores. $Q_{liq\ water}$ corresponds to water injection in liquid phase, Q_{comp} corresponds to injection in vapour phase from vapour saturated pores, Q corresponds to injection in vapour phase from inlet dry pores (see text). (For interpretation of the references to color in this figure legend, the reader is referred to the web version of this article.)

(5) Then, a second nucleation step is performed. The procedure is the same as in step #3 but is performed for the inlet boundary conditions specified in step #4.

(6) All the liquid clusters present in the network grow simultaneously. For a given liquid cluster no new dry element at the interface with the cluster can be invaded until all of the elements of the liquid cluster are fully saturated. If several elements at the boundary of the liquid cluster are partially saturated, the water flux entering the cluster is distributed evenly between these elements. Once all the elements of a given cluster are fully saturated, the dry boundary element with the largest equivalent diameter is selected as the next one to be invaded. After every new invasion, the temperature and water vapour molar fraction fields are updated and a nucleation step is carried out. This liquid cluster growth step continues until every liquid cluster has reached the injection-condensation-evaporation equilibrium. For a given cluster, this equilibrium means that the mass flow rate of water injected in liquid phase at the GDL inlet and entering the cluster, if any, the mass flow rate of water feeding the cluster by condensation and the mass flow rate of water leaving the cluster by evaporation are balanced. When the equilibrium is reached for each cluster, the steady –state is considered as having being reached and the procedure stops.

3. Calibration of MIPNM

3.1. Parametrization of liquid injection point fraction

The fraction of injection points α is an input parameter for the model. Considering that the liquid injection takes place in a limited number of inlet pores can be related to the impact of the MPL which induces preferential pathways for the liquid water transport. This phenomenon can be even more marked in the presence of cracks along the through-plane direction of the MPL. It can be surmised that the number of injection points varies depending on the thickness of the MPL and/or the presence of cracks in the MPL. Even in the absence of MPL, it is quite reasonable to consider that the water produced in the CL enters the GDL only through a fraction of the pores of the GDL in contact with the CL. However, direct estimates for this parameter are not available in the literature. In the case of the pure liquid injection scenario ignoring the phase change phenomena, it has been shown that this parameter has an impact on the number of breakthrough points and thus on the number of liquid clusters forming in the network, e.g. [43]. In order to assess the impact of this parameter for the Mixed Injection Pore Network Model (MIPNM), preliminary comparisons were performed with available experimental results considering four reasonable values of α, namely 5%, 10%, 20% and 30%. The experimental results chosen to perform the calibration were the ones from Eller et al. [6] ($T_{bp} = 80$ °C, $i = 0.75$ A·cm^{-2}, $RH_{ch} = 100\%$). The calibration was performed from the computation of the saturation profiles (in-plane, through-plane under the rib and through-plane under the channel; in a given domain, i.e. a slice, the saturation is the volume fraction of the pore space occupied by liquid water). The simulations led to trends in the saturation profiles in qualitative agreement with the experimental data for the four considered values of α. As illustrated in Fig. 3a, the impact of α on the through-plane saturation profile is mostly on the saturation at the GDL inlet. Also, as illustrated in Fig. 3b, increasing α mostly increases the saturation in the region below the channels. Varying the liquid injection point fraction α enables one to match the through-plane saturation values at the bottom and top layers of pores in the different regions. A too low value of α like 5% or 10% leads to too low in-plane saturation levels under the channel and too low through-plane saturation in the first layer of pores com-
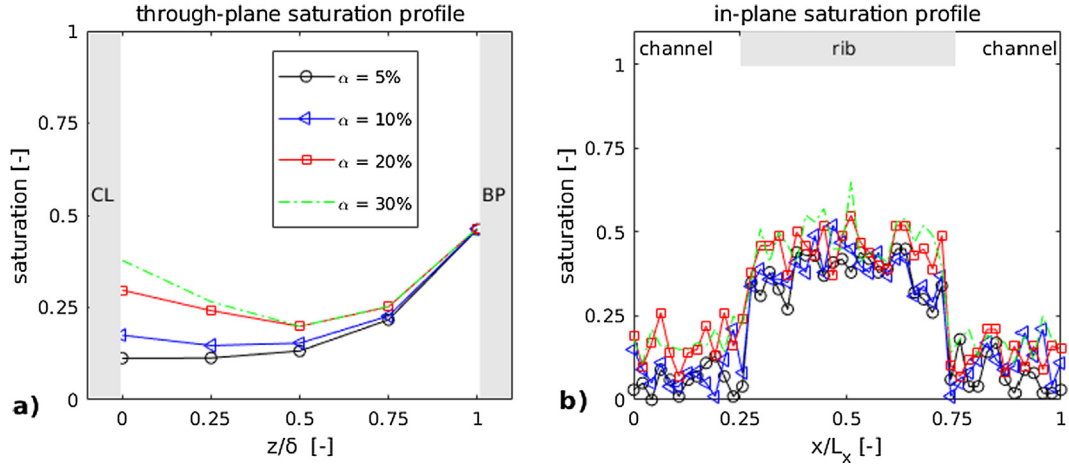
Fig. 3. Impact of α on the through-plane (a) and in-plane (b) saturation profiles. (T_{bp} = 80 °C, i = 0.75 A·cm^{-2}, RH_{ch} = 100%).
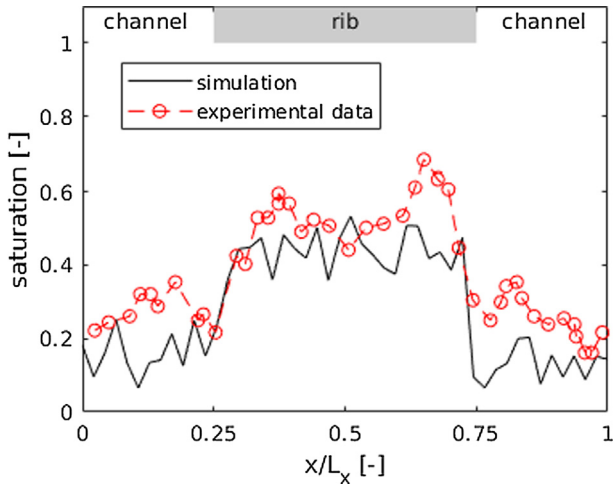

Fig. 4. In-plane saturation profiles obtained with the MIPNM (α = 20%) compared to the experimental data available in [6] (Case A03 in this Ref. T_{bp} = 80 °C, i = 0.75 A·cm^{-2}, RH_{ch} = 100%). The transverse coordinate x is made dimensionless using the total width of GDL unit cell.

pared to the experimental results [6]. As illustrated in Fig. 4, choosing α = 20% leads to a fair match with the experimental data. For this value, the agreement between experimental results and numerical predictions is good. Not only the trends are the same but the saturation levels in the different regions also agree. The through-plane saturation profiles are depicted in Fig. 5. They are in quite reasonable agreement with the liquid water distribution shown in [6] as colour map (see Fig. 6 A03 in [6]). The saturation increases in the region under the rib from the GDL inlet up to a maximum value close to the rib while the saturation decreases in the region under the channel to reach values close to 0 at the interface with the gas channel.

3.2. Parametrization of the network anisotropy

The chosen moderately anisotropic pore network structure is also a feature that can be discussed. Although it is known that GDLs are anisotropic fibrous materials, it is not so obvious to specify the throat size distributions in the through-plane and in-plane directions of the network. The experimental results available in the literature do not make a distinction between the through-plane and in-plane directions, nor actually between pore sizes
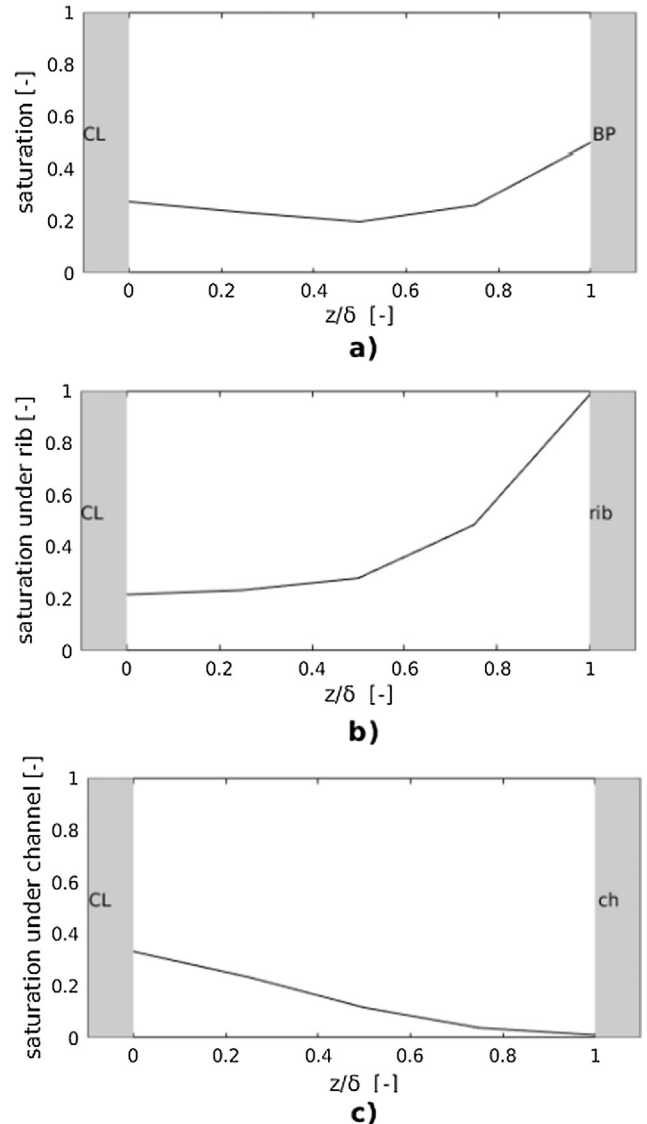

Fig. 5. Computed water saturation profiles obtained for α = 20% simulating the experimental case A03 in [6]: through-plane (a), through-plane under the rib (b) and through-plane under the channel (c). The GDL inlet is at $z/\delta = 0$; the rib and channels (BP) are at $z/\delta = 1$. (T_{bp} = 80 °C, i = 0.75 A·cm^{-2}, RH_{ch} = 100%).

and throat sizes. In order to check that the chosen structure was acceptable, simulations were performed with the MIPNM and $\alpha = 20\%$ changing the anisotropy of the network. In addition to the network described in Section 2 and used for the simulations presented in Section 3.1, referred to as moderately anisotropic, simulations were also performed with a highly anisotropic pore network structure and an isotropic one. Note that anisotropy here refers only to the throat size distributions (TSD) in the through-plane and in-plane directions (the properties indicated in Table 1 were not modified). Thus isotropic means the same TSD in the three directions of the network whereas highly anisotropic means no overlap between the in-plane TSD and through-plane TSD. These simulations have indicated that the structure defined in Section 2 was appropriate. Indeed, the degree of anisotropy of the GDL has a significant impact on the liquid water distribution in the different regions of the GDL, namely below the rib and below the channel. A valuable indicator in this respect to specify the most appropriate structure is the ratio between the mean saturation under the channel and the mean saturation under the rib. For almost isotropic structures this ratio tends toward 1 while it tends towards 0.2 for the most anisotropic structure simulated. According to the experimental data available in [6], this ratio ranges from 0.3 to 0.4 for the operating conditions considered. The simulations made with MIPNM for the moderately anisotropic structure lead to a ratio of 0.31. Thus in what follows, the moderately anisotropic network is used and $\alpha = 20\%$ unless otherwise mentioned.

4. Comparison between the different models and experimental results

As indicated in the introduction, two main kinds of PNM have been used so far to simulate the filling of the cathode GDL pore space by liquid water. The first one, referred to as LIPNM, is based on the assumption that water enters the cathode GDL in liquid form under isothermal conditions without consideration of liquid-vapour phase change phenomena. The second one, referred to as CPNM, assumes that the water generated by electrochemical reaction enters the GDL in vapour phase and diffuses within the pore network as the result of the vapour molar fraction difference between the GDL inlet and the bipolar plate channels. The pore filling by liquid water, if any, is by condensation of the vapour. The third option is the mixed scenario presented in the present article (MIPNM). In the latter, water can enter the GDL in vapour phase but also in liquid phase in a finite number of injection points depending on the conditions at the GDL inlet.

In this section, two quite distinct operating conditions are first considered so as to compare the results obtained with the three models with a focus on the fully humidified conditions in the channel ($RH_{ch} = 100\%$). The first one corresponds to a relatively low operating temperature ($\sim 40\,^\circ$C) whereas the second corresponds to a standard operating temperature ($\sim 80\,^\circ$C). Then the case of an intermediate operating temperature ($\sim 60\,^\circ$C) is considered using the MIPNM.

4.1. Low operating temperatures ($\sim 40\,^\circ$C)

The low temperature case corresponding to the conditions imposed by Eller et al. [5] in their low temperature X ray tomography experiment ($T_{bp} = 40\,^\circ$C, $i = 0.5$ A·cm^{-2}, $RH_{ch} = 100\%$) is illustrated in Fig. 6. This case is characterized by the presence of liquid water both below the rib and below the channel. For the pure liquid injection (LIPNM) and mixed vapour/liquid injection (MIPNM) models, the liquid injection point density has been set to $\alpha = 20\%$. As can be seen, both the LIPNM and MIPLM lead to a liquid water distribution qualitatively similar to the experimental
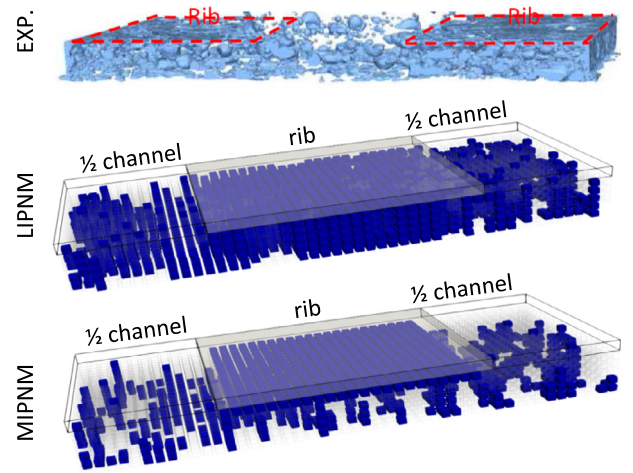

Fig. 6. Liquid water distributions for a low operating temperature and fully humidified conditions in the channel ($T_{bp} = 40\,^\circ$C, $i = 0.5$ A·cm^{-2}, $RH_{ch} = 100\%$). The top image is the experimental distribution obtained by Eller et al. [5] from X-ray tomography (reproduced with permission from *J. Electrochem. Soc.*, 158, 8 (2011). Copyright 2011, The Electrochemical Society). Note that the channel is in the middle and ribs are on the side in the experiment, contrary to the simulations where the rib is in the middle. The image in the middle shows the distribution obtained with the LIPNM ($\alpha = 20\%$). The image at the bottom show the distribution obtained with the MIPNM ($\alpha = 20\%$).

one. However, the mean saturation level is different between the two models. The pure liquid injection model predicts higher saturation levels, especially under the rib. This difference can be explained by the fact that the water condensation in the GDL right under the rib predicted by the MIPNM helps the different liquid injection clusters to quickly form a unique cluster under the rib before invading other network elements, i.e. pores or throats. Furthermore, injection-condensation-evaporation equilibrium is reached in some liquid clusters located under the channel region before breakthrough. This phenomenon contributes to reduce the saturation in this region compared to the prediction of the LIPNM ignoring the liquid-vapour phase change phenomena. Although it is not easy to decide from the comparison shown in Fig. 6 which simulated distribution is the closest to the experimental one, it can be noted that the latter suggests that some liquid clusters are not connected to the inlet or to the channel. This feature is not possible with the LIPNM. Therefore, we conclude that the mixed liquid/vapour injection model (MIPNM) looks in better agreement with the experimental observations from Eller et al. [5]. We have not shown for this case the distribution obtained with the CPNM. The latter actually predicts that the first slice of pores at the inlet is fully saturated. This is not consistent since this would fully block the oxygen access to the CL and different from the experimental visualisation (top view in Fig. 6), which clearly suggests that the first slice of pores is only partially saturated, especially below the channel, as also predicted with the MIPNM.

4.2. Standard operating temperatures ($\sim 80\,^\circ$C)

The second operation conditions that have been simulated are the one corresponding to Eller et al. experiments [6] at standard operating temperature ($T_{bp} = 80\,^\circ$C, $i = 0.75$ A·cm^{-2}). As illustrated in Fig. 7, note that in this particular experiment the rib is twice as large as the channel. This has been taken into account in the simulations. We first consider the case where the channel gas is not fully humidified ($RH_{ch} \sim 80\%$). The experimental distribution of liquid water is shown in Fig. 7 together with the distributions predictions by the various models. As for the distributions discussed in [26], the experimental distribution is characterized in
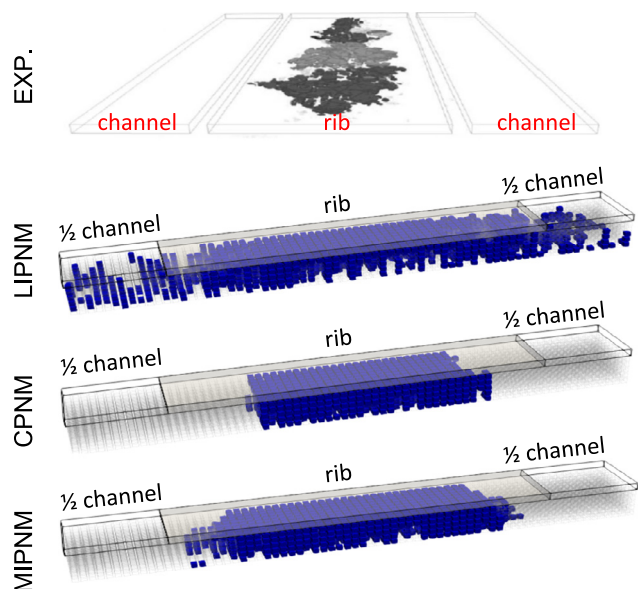
Fig. 7. Liquid water distributions for a standard operating temperature and humidity conditions in the channel less than 100% (T_{bp} = 80 °C, i = 0.75 A·cm^{-2}, RH_{ch} = 80%). Comparison between the experimental distribution obtained by Eller et al. [6] from X-ray tomography (top image) (reproduced with permission from authors.) and the distribution obtained from the various PNMs, namely LIPNM (α =20%), CPNM and MIPNM (α =20%).

this case by a strong separation between the channel and the rib. This means that liquid water is present only in the region of the GDL below the rib with no liquid water below the channels. In accordance with the simulations presented in [26], the condensation PNM (CPNM) well captures the separation effect. Interestingly, as depicted in Fig. 7, the mixed injection model also leads to a strong separation effect as in the experiment. However, the liquid water is a bit less confined below the central region of the rib than with the CPNM. This is a consequence of the fact that some water is injected in liquid phase at the inlet with the MIPNM. The MIPNM liquid water distribution seems to be in a better agreement with the experimental distribution than the one obtained with the CPNM. It is clear from Fig. 7 that the pure liquid injection model (LIPNM) is totally inappropriate for these operating conditions.

Liquid water distributions when the gas in the channels is fully humidified (RH_{ch} = 100%) for this operating temperature (80 °C) are shown in Fig. 8. As can be seen, the liquid water distribution obtained in the experiment presented in [6] for this case is characterized by the presence of liquid water both in the region of the GDL below the rib and also below the channels. This distribution is therefore markedly different from the one observed for RH_{ch} = 80% (Fig. 7). The pure liquid injection model (LIPNM) looks inappropriate for these conditions since the fraction of liquid pores looks noticeably higher than in the experiment. The pure vapour injection model (CPNM) leads to worse results. It predicts a strong separation effect between rib and channel except over the first layer of pores which is completely flooded. This is clearly not consistent with the experimental distribution. The best results are clearly obtained using the mixed liquid/vapour injection model (MIPNM). This model predicts the presence of condensed water right under the rib, the presence of liquid injected water under the channel region and no flooding of the GDL. For this second case also, the new model is the more relevant to predict what happens during the experiments.

Then the MIPNM model was tested as regards the impact of the rib width/channel width ratio. This ratio is one for the reference case (rib width equal to channel width). Interestingly, experimen-
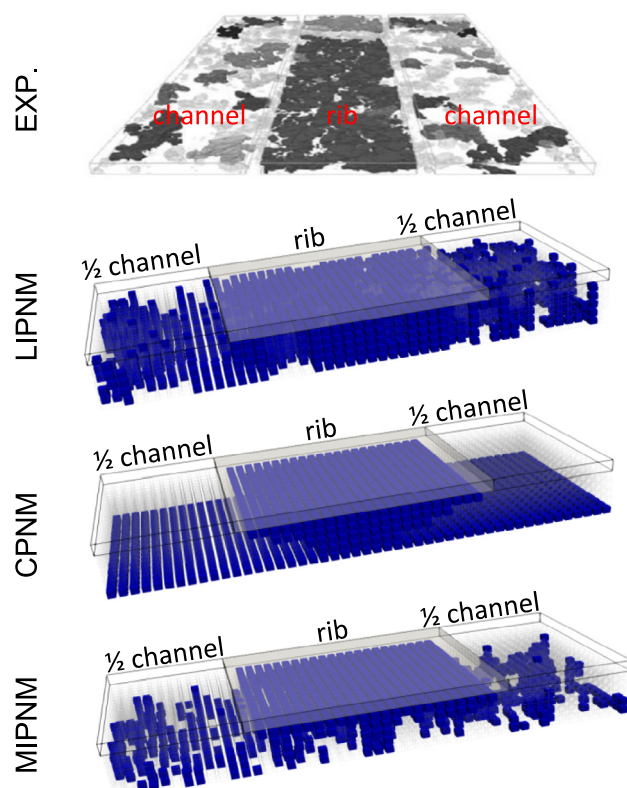

Fig. 8. Liquid water distributions for a standard operating temperature and fully humidified conditions in the channel (T_{bp} = 80 °C, i = 0.75 A·cm^{-2}, RH_{ch} = 100%). Comparison between the experimental distribution obtained by Eller et al. [6] from X-ray tomography (top image, the various liquid clusters are shown using various levels of grey) (reproduced with permission from authors.) and the distribution obtained from the various PNMS, namely LIPNM (α = 20%), CPNM and MIPNM (α = 20%).

tal visualisations of the liquid water distributions are presented in Eller et al. [6] for the standard case where the ratio is one but also for a ratio of 2 (rib width twice as large as channel width), referred to as the special geometry. The numerical distributions are depicted in Fig. 9. They are in good agreement with the experimental results [6]: no liquid water in the GDL for the basic rib/channel geometry and RH_{ch} = 80%, liquid water present only under the rib for the special rib/channel geometry at RH_{ch} = 80% and finally, presence of liquid water in every region for special rib/channel geometry at RH_{ch} = 100% with a peak of saturation under the rib.

4.3. Intermediate operating temperatures (∼60 °C, RH_{ch} = 100%)

In situ observations of liquid water distribution in fuel cells operating at an intermediate temperature of 60 °C have been presented in [7,8]. The current density was 1.5 A·cm^{-2} in the experiments reported in [8] while the experiments in [7] were at the limiting current density, close to 2.5 A·cm^{-2}. Another difference lies in the bipolar plate design. The channel width was 0.2 mm in [8], which is very narrow, while this width was 0.5 mm in [7]. Considering the respective geometry of both cases leads to a network of 24 × 20 × 4 pores for the configuration of [7] and to a network of 10x10x5 pores for the configuration studied in [8].

The same calibration work as for Eller et al. [6] data has been performed for the experimental case RH_{ch} = 100% from [7]. The heat flux was reduced from 0.5Φ to 0.4Φ to obtain better results. This change can be justified by the fact that the produced heat is partially removed from the fuel cell by a water-coolant circulation
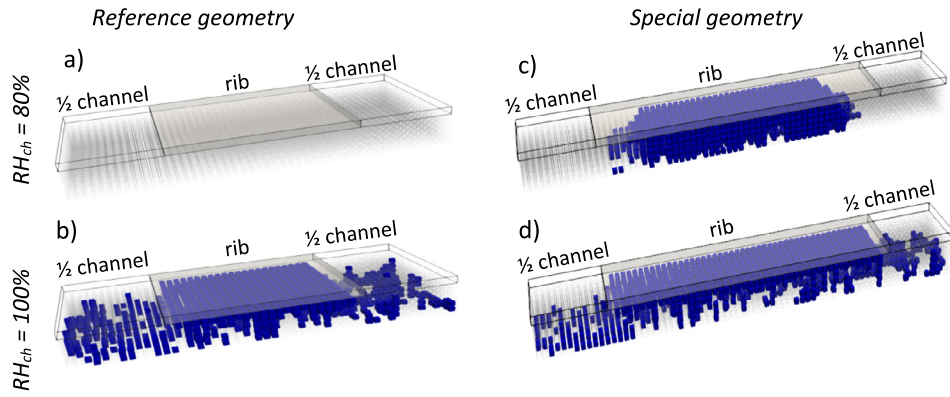
Reference geometry

Special geometry

Fig. 9. Liquid water distributions obtained using the MIPNM ($\alpha = 20\%$) for an operating temperature $T_{bp} = 80$ °C and a current density $i = 0.75$ A·cm^{-2} in a cathode GDL unit cell located under a bipolar plate with $L_r = L_{ch}$ (cases a, b) and a bipolar plate with the rib width twice as large as the channel width ($L_r = 2L_{ch}$) (cases c, d).
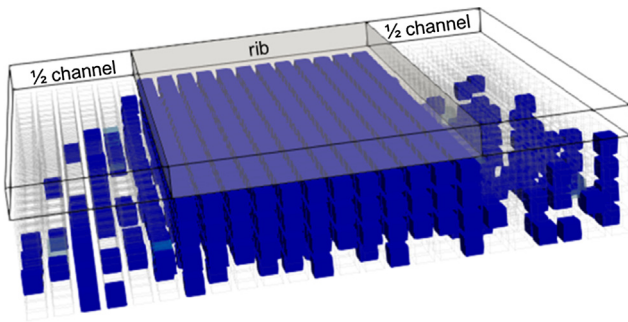

Fig. 10. Liquid water distribution obtained with the MIPNM ($\alpha = 10\%$) for the conditions of Muirhead et al. [7] ($T_{bp} = 60$ °C, $i = 2.5$ A.cm^{-2}, $RH_{ch} = 100\%$).

system in this experiment [7]. A value of $\alpha \approx 10\%$ gives saturation levels at the GDL/MPL interface in reasonable agreement with the experimental results (Fig. 11). The liquid distribution computed

with the MIPNM for those conditions is shown in Fig. 10. The computed through-plane saturation profiles are depicted in Fig. 11. First, under the rib region, the mean saturation increases from the GDL inlet up to a maximal value under the rib where the GDL is almost flooded. Secondly, in the region under the channel, the saturation increases from the GDL inlet to the second layer of pores and then decreases up to the channel. The saturation levels are in reasonable agreement with the experimental ones for the region under the channel. However, the numerical values are too high under the rib. Explanation for this difference is proposed in Section 5.

In the experiments in [8], the reactant gas relative humidity was varied in the range [25%, 50%, 75%, 100%]. As for the simulation of Muirhead et al.'s experiment [7], the heat flux was reduced to 0.4Φ given the fact that a water bath cooling system was also used. All these relative humidity conditions have been simulated. Results are illustrated in Fig. 12. The MIPNM predicts
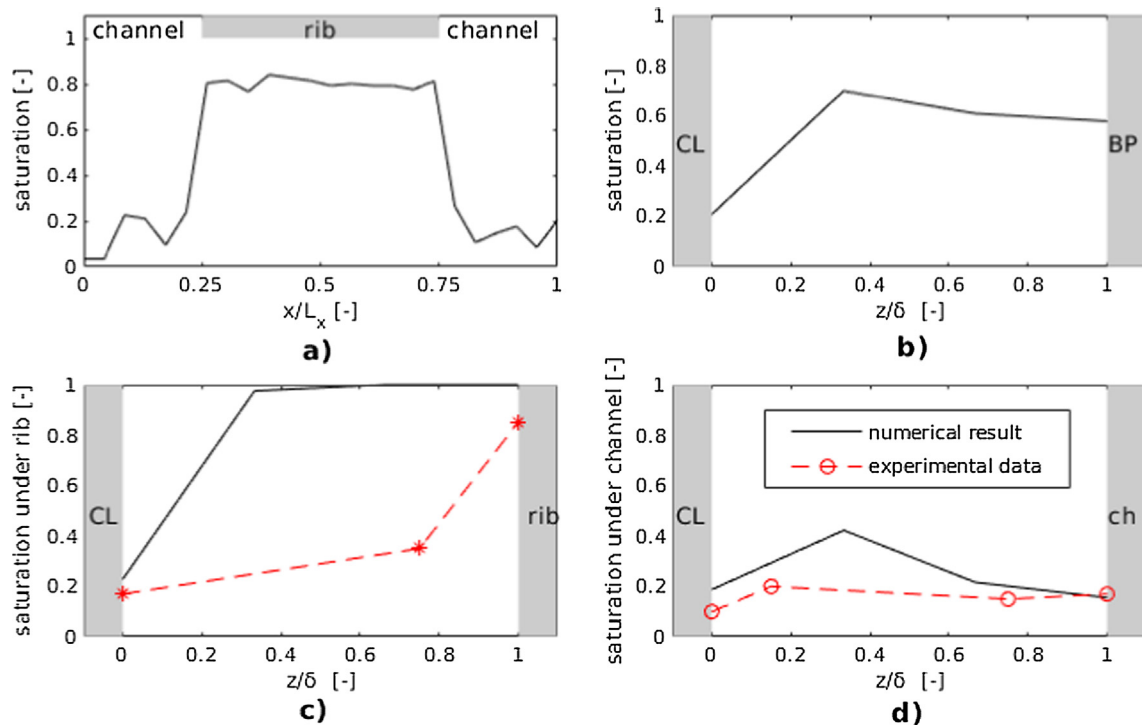

Fig. 11. Water saturation profiles obtained with the calibrated MIPNM (black curves; $\alpha = 10\%$) and adapted experimental data (dashed lines with symbols in red) from [7]: in-plane (a), through-plane (b), through-plane under the rib (c) and through-plane under the channel (d). ($T_{bp} = 60$ °C, $i = 2.5$ A.cm^{-2}, $RH_{ch} = 100\%$).
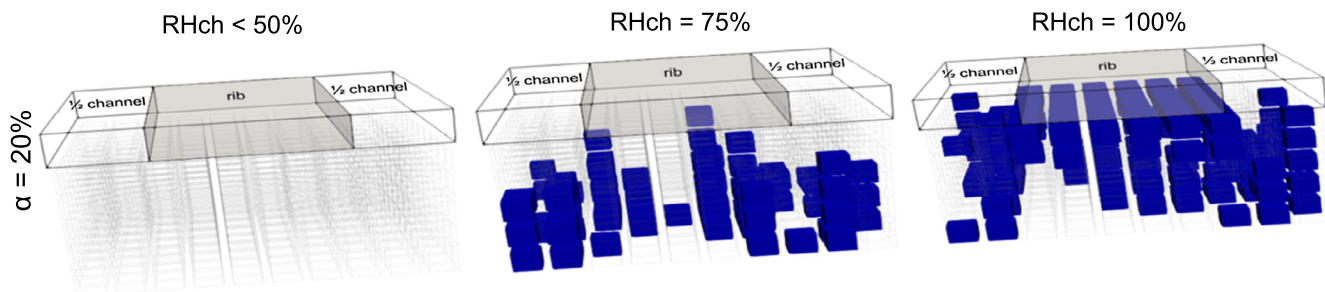
Fig. 12. Liquid water distribution obtained for the simulation of Chevalier et al.'s experimental conditions [8] (T_{bp} = 60 °C, i = 1.5 A.cm^{-2}) using MIPNM (α = 20%).
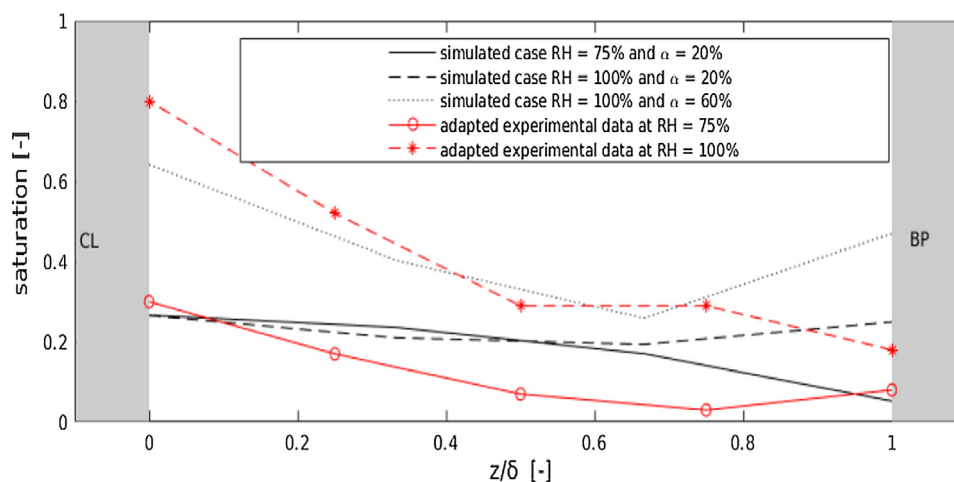

Fig. 13. Through-plane saturation profiles obtained when simulating Chevalier et al. experimental cases [7] (black) and reported corresponding experimental data (red) (T_{bp} = 60 °C, i = 1.5 A.cm^{-2}). (For interpretation of the references to color in this figure legend, the reader is referred to the web version of this article.)

a global evolution of the liquid water distribution with reactant gas relative humidity in good agreement with the experimental results from [8]. For low relative humidity conditions, meaning 25% and 50%, it is found that the cathode GDL remains dry. Chevalier et al. [8] reported that the GDL also remained dry at RH_{ch} = 25% but a small amount of liquid water could be found at RH_{ch} = 50%, mainly at the interface with the MPL. For higher relative humidities, the simulations predicted the presence of liquid water in agreement with the experiment. As illustrated in Fig. 13, applying a density of liquid injection points α equal to 20% leads to a mean saturation level in the first layer of pores agreeing with the experimental one estimated in [8] at RH_{ch} = 75%. Finally at RH_{ch} = 100%, the model predicts the formation of liquid water in the GDL by condensation in the pores close to the rib and by liquid injection at the MPL/GDL interface. This leads to higher saturation levels compared to the ones obtained at RH_{ch} = 75%. Setting α to 60% permits to obtain the desired level of water saturation at the GLD/MPL interface for this case (Fig. 13). However, as illustrated in Fig. 13, the simulation does not predict exactly the same water saturation profile in the through-plane direction. Indeed, while Chevalier et al. [8] reported a continuous decrease from the GDL inlet up to very low values at the bipolar plate/GDL interface, our model predicts a less drastic decrease in the first layers of pores followed by an increase in the last layer of pores where water is formed by condensation. Some possible explanations are discussed in Section 5.

5. Discussions

The conclusion is therefore that the mixed injection model (MIPNM) leads to results in good agreement, at least qualitative, with experimental observations for all the operating conditions considered. Compared to previous models, it is able to predict consistent liquid distributions for a large range of operating conditions: low, intermediate and standard operating temperature, fully or partially humidified gas in the channel. It reconciles the previous works, since it leads to liquid water distributions resembling the ones predicted by the first group of PNM (referred to as LIPNM) when the temperature is low and the gas fully humidified and the liquid distributions predicted by the condensation PNM (CPNM) for the sufficiently high operating temperatures and gas in the feeding channel with a relatively humidity less than 100%. Furthermore, it leads to results more consistent with the experiment than the LIPNM at low temperature. However, the comparison with the liquid experimental distribution at 60 °C was a bit less good. Nevertheless many important trends were well reproduced by the model also for this operating temperature. Several explanations can be proposed as regards some of the discrepancies observed between the model and the experiments. First of all, uncertainties are necessarily associated with the type of experiments leading to the results discussed in Section 4. The discrepancies might be due in part to experimental artefacts. The results presented in [7] or [8] also suggest that the porosity significantly

varies over the GDL thickness. This feature has not been taken into account in our simulations. Also, it should be pointed out that a special design of bipolar plate with a rib width of only 200 μm was used in [8]. This leads to only 5 pores over the rib width in our model since we kept the lattice spacing unchanged (40 μm) in all the simulations. So perhaps, works should be performed for defining the pore network model properties so as to be more representative of the particular fuel cells used in [8]. Also, it is known that the current density is actually not uniform at the GDL inlet and can be significantly less below the rib, e.g. [44]. This effect is not taken into account in our simulations. This might explain the greater saturation obtained under the rib in the simulations for the case illustrated in Fig. 11. The occurrence of condensation is strongly dependent on the heat transfer. Thus, in addition to the possible non uniform inlet current density condition at the GDL, the heat and mass transfer properties used in the simulations are perhaps not sufficiently representative of the experimental situation considered in [8].

In this respect, we recall that two noticeable modifications were introduced compared to the heat transfer model presented in [26]. As for the PNM described in [28], the latent heat transfer associated with the liquid-vapour phase change is taken into account in pores where phase change occurs. Condensation releases heat while evaporation induces some local cooling. The second modification lies in the dependence of the local thermal conductivity with saturation. So far, this feature had never been implemented in GDL PNMs. The impact of the two modifications was studied separately as well as together for different operating conditions. On the whole, the latent heat transfer tends to warm up the GDL while the dependence of thermal conductivity with water saturation tends to cool it. The simulation of a low temperature and low current density case (T_{bp} = 40 °C, i = 0.5 A·cm^{-2}, RH_{ch} = 100%) led to the conclusion that the introduced modifications, separately or together, have no significant impact on the liquid water distribution compared to the simulation made without considering these two effects. By contrast, the simulation for high temperatures, i.e. close to the standard operating temperature and moderate current densities, i.e. T_{bp} = 80 °C, i = 0.75 A·cm^{-2}, RH_{ch} = 100%, leads to a reverse conclusion. Indeed, the obtained liquid water distributions depend on

the heat transfer model assumptions. In the region located under the channel, the consideration of both improvements leads to an increase in the water saturation. This can be explained by the fact that the region is colder both because of the higher conductivity due to the liquid water presence and the cooling effect due to evaporation. The slightly lower temperatures in this region favour the growth of liquid clusters. Conversely, in the region under the rib where clusters are initially formed by condensation, the warming effect due to condensation contributes to reduce the water saturation, see also [28]. It can be concluded that the above-mentioned modifications have a non-negligible impact and should be systematically incorporated in the modelling of transfers in GDL under in-situ conditions.

Also, it can be noted that our model does not explicitly consider the presence of a MPL. Regarding the experiments, a MPL was present in the experiments discussed in Sections 3.1, 4.2 and 4.3 but not in the experiment discussed in Section 4.1. In this respect, it would be interesting to consider explicitly the MPL in the modelling.

The MIPNM as well as the LIPNM involves the input parameter α (fraction of liquid injection pores at the GDL inlet). For the moment, this is essentially a calibration/fitting parameter. It would be interesting to develop experimental and/or numerical works aiming at characterizing this parameter. One option to specify this parameter and to study the influence of various factors (current density, relative humidity, temperature...) on its value could be to develop a much more comprehensive model coupling the present model with models describing the transfers in the other layers (MPL, CL, membrane, etc.).

6. Operating regime diagram

The concept of condensation diagram was introduced in [26] to delineate the conditions leading to the formation of liquid water by condensation when the GDL pore filling by liquid water is actually due to condensation only (no liquid water injection at the inlet). This diagram shows that two main cases can happen at the standard operating temperature (∼80 °C). In the first case, the GDL remains dry and all the produced water is transferred in vapour phase. This regime is expected for a sufficiently low current density
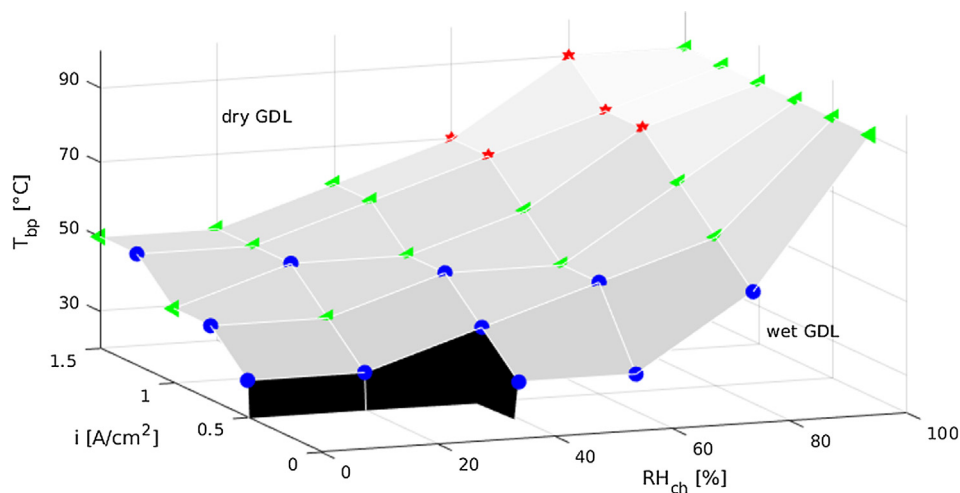
Fig. 14. Cathode GDL operating regime 3D diagram from MIPNM simulations (α = 20%): the surface corresponds to the boundary between the dry GDL region conditions and the wet GDL conditions. The blue circles corresponds to operating points for which the GDL pore filling by liquid water is due to liquid water injection at the inlet only whereas red stars correspond to operating conditions for which liquid water forms by condensation only. For the operating points below the surface in the wet GDL region, the pore filling by liquid water results from both mechanisms. (For interpretation of the references to color in this figure legend, the reader is referred to the web version of this article.)

and/or a sufficiently low relative humidity in the channel. In the second case, condensation happens and some pores are filled with liquid water in the region under the rib. This regime is expected for a sufficiently high current density and/or a sufficiently high relative humidity in the channel.

An extension of this diagram is proposed in what follows so as to take into account all the regimes identified using the new PNM (MIPNM). To this end, simulations were performed for the following conditions: T_{bp} between 30 °C and 90 °C, i between 0.25 A.cm^{-2} and 1.5 A.cm^{-2} and RH_{ch} between 0% and 100%. A total of 252 different cases were computed.

This leads to the 3D operating regime diagram depicted in Fig. 14. The surface plotted in Fig. 14 separates the operating conditions corresponding to a dry GDL from the ones leading to the presence of liquid water in the GDL. The operating points above the surface correspond to a dry GDL. In the corresponding regime, the water enters the GDL in vapour form and is transferred through the GDL in vapour form up to the channel. The operating points below the surface correspond to a GDL containing liquid water. The lower is the temperature or the higher is the current density or the higher is the channel relative humidity, the more likely liquid water is present in the GDL. Depending on the conditions, liquid water forms by condensation only, as a result of liquid injection at the inlet only or as a result of both liquid injection at the GDL inlet and condensation. In most wet cases, the two mechanisms happen simultaneously. However, for some operating conditions, only one of these two mechanisms is responsible for the liquid water presence. These conditions are only met at the boundary surface between the dry GDL region and the wet GDL region in the diagram. The operating points for which the filling of pores by liquid water is due to condensation only are marked by a red star in Fig. 14. It can be seen that this only happens for a sufficiently high temperature (from 70 °C to 90 °C), a not too high relative humidity (60–80%) and a sufficiently high current density (1–1.5 A.cm^{-2}). These operating conditions are close to the ones considered by Straubhaar et al. [26] for the development of their condensation pore network (CPNM). The presence of liquid water due to liquid water injection only happens for a sufficiently low temperature (from 30 °C to 50 °C), a low to high relative humidity (from 0% to 80%) and low to high current densities (from 0.25 to 1.25 A.cm^{-2}). For this regime, it can be noted that the model predicts that the liquid water injection points are mainly located in the region of the GDL inlet under the rib whereas no water is injected in liquid form at the inlet in the region below the channels.

The liquid water formation conditions have a significant impact on the liquid water distribution and on the liquid water saturation level. The operating conditions corresponding to pure liquid injection regime or to the pure condensation regime lead to the smaller amount of liquid water, with the liquid water located only in the region under the rib. By contrast, the operating conditions corresponding to the regime where the pore filling by liquid water results from both condensation and liquid injection leads to higher saturation levels with the presence of liquid water in every region of the GDL, i.e. below the rib and below the channels.

In summary, the operating regime diagram identifies four regimes, namely the dry regime, the dominant condensation regime, the dominant liquid injection regime, the mixed regime where both the capillarity controlled invasion in liquid phase from the adjacent layer (MPL or CL) and condensation inside the GDL are important.

7. Conclusions

We have studied the water transfer on the cathode side of a PEM fuel cell from pore network simulations. To this end, we have first developed a new PNM, referred to as the Mixed Injection Pore Network Model (MIPNM), combining injection in liquid phase into the GDL through a fraction of inlet pores and liquid phase change phenomena (evaporation–condensation). This model reconciles the previous PNMs since it is able to simulate both the situations where liquid injection is an important feature and the situations where pore filling by liquid water is only due to condensation. The model is also able to simulate the conditions when gas in the channel is fully humidified where both the liquid injection in liquid phase and the condensation process must be taken into account together.

Comparisons with liquid water distributions presented in the literature are quite encouraging and indicate that the MIPNM is able to simulate a quite large range of operating conditions.

This led to identify several operating regimes which can be summarized in a diagram depending on the mean current density, the operating temperature and the relative humidity in the channel. The four main regimes so identified are: a regime where the GDL is fully dry and the water transfer in vapour phase only, a regime where liquid water pore filling is due to water vapour condensation only, a regime where liquid water pore filling results from injection in liquid phase at the GDL inlet only (this regime is expected at low temperature only) and a mixed regime where liquid water pore filling is due to both liquid injection at the inlet and vapour condensation inside the GDL (especially in the rib area).

This model can be extended in various directions. As in [27], it would be interesting to couple it with the oxygen transport and the electronic transfer. Also, coupling with the transfers in the other layers, including the anode side, would be interesting in the prospect of understanding in more depth the water transfers in PEM fuel cells.

Conflict of interests

All authors will disclose any actual or potential conflict of interest including any financial, personal or other relationships with other people or organizations within three years of beginning the submitted work that could inappropriately influence, or be perceived to influence, their work.

Appendix A.

See Fig. A1.

Fig. A1. Flow chart of MIPNM algorithm.

Dry GDL

Compute T, x_{H2O} and RH fields in network

Nucleation step (identification of "condensation" elements in network)

DO WHILE max$\{RH(i,j,k)\} > \eta$
- Identify element (i,j,k) of maximal RH and set it as condensation element
- Compute T, x_{H2O} and RH fields

Set inlet BC

- Randomly chose liquid injection points among condensation elements at inlet
- Set RH=100% in inlet condensation elements non-chosen as liquid injection points
- Set the computed RH to remaining elements at inlet

Nucleation step (identify condensation element, if any)

Liquid cluster growth step

IF not all the element of the cluster are filled
- Fill the elements

ELSE
- Invade the boundary element of largest equivalent diameter

END IF
Compute T, x_{H2O}, and RH field

Equilibrium ?

rib

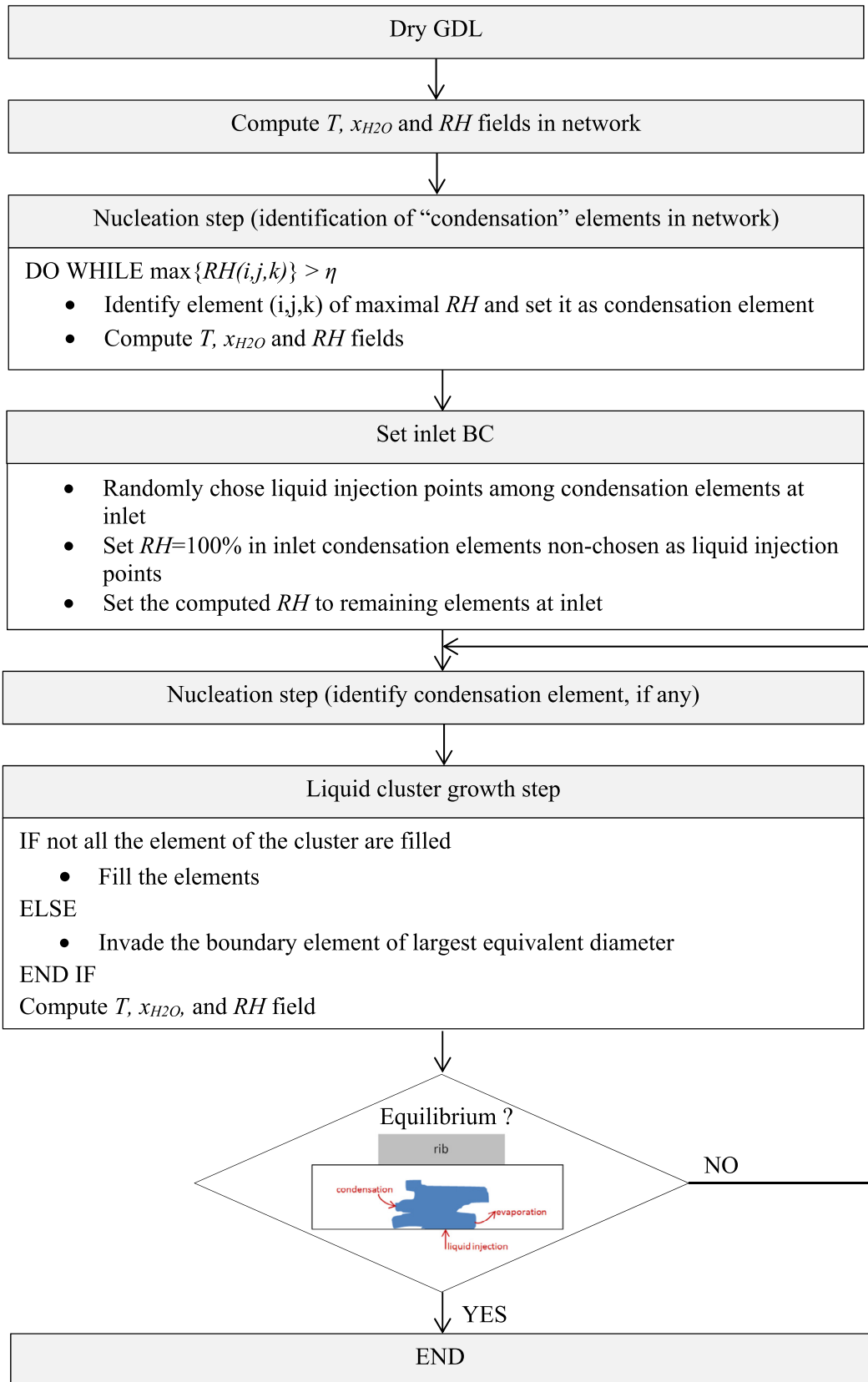condensation   evaporation

liquid injection

NO

YES

END

Fig. A1. Flow chart of MIPNM algorithm.

Appendix B. Supplementary material

Supplementary data associated with this article can be found, in the online version, at https://doi.org/10.1016/j.ijheatmasstransfer. 2018.10.004.

References

[1] M. Eikerling, A.A. Kornyshev, A.R. Kucernak, Water in polymer electrolyte fuel cells: friend or foe?, Phys Today 59 (2006) 38.

[2] F. Nandjou, J.-P. Poirot-Crouvezier, M. Chandesris, J.-F. Blachot, C. Bonnaud, Y. Bultel, Impact of heat and water management on proton exchange membrane fuel cells degradation in automotive application, J. Power Sources 326 (2016) 182–192.

[3] T. Jahnke, G. Futter, A. Latz, T. Malkow, G. Papakonstantinou, G. Tsotridis, P. Schott, M. Gérard, M. Quinaud, M. Quirog, A.A. Franco, K. Malekh, F. Calle-Vallejo, R. Ferreira de Morais, T. Kerber, P. Sautet, D. Loffreda, S. Strahl, M. Serra, P. Polverino, C. Pianese, M. Mayur, W.G. Bessler, C. Kompis, Performance and degradation of proton exchange membrane fuel cells: state of the art in modeling from atomistic to system scale, J. Power Sources 304 (2016) 207–233.

[4] M. Sabharwal, J.T. Gostick, M. Secanell, Virtual liquid water intrusion in fuel cell gas diffusion media, J. Electrochem. Soc. 165 (7) (2018) 553–563.

[5] J. Eller, T. Rosén, F. Marone, M. Stampanoni, A. Wokaun, F.N. Büchi, Progress in in situ X-ray tomographic microscopy of liquid water in gas diffusion layers of PEFC, J. Electrochem. Soc. 158 (8) (2011) 963–970.

[6] J. Eller, J. Roth, F. Marone, M. Stampanoni, F.N. Büchi, Operando properties of gas diffusion layers: saturation and liquid permeability, J. Electrochem. Soc. 164 (2017) 115–126.

[7] D. Muirhead, R. Banerjee, J. Lee, M.G. George, N. Ge, H. Liu, S. Chevalier, J. Hinebaugh, K. Han, A. Bazylak, Simultaneous characterization of oxygen transport resistance and spatially resolved liquid water saturation at high-current density of polymer electrolyte membrane fuel cells with varied cathode relative humidity, Int. J. Hydrogen Energy (2017), https://doi.org/10.1016/j.ijhydene.2017.10.031.

[8] S. Chevalier, J. Lee, N. Ge, R. Yip, P. Antonacci, Y. Tabuchi, T. Kotaka, A. Bazylak, In operando measurements of liquid water saturation distributions and effective diffusivities of polymer electrolyte membrane fuel cell gas diffusion layers, Electrochim. Acta 210 (2016) 792–803.

[9] J.M. LaManna, S. Chakraborty, J.J. Gagliardo, M.M. Mench, Isolation of transport mechanisms in PEFCs using high resolution neutron imaging, Int. J. Hydrogen Energy 39 (2014) 3387–3396.

[10] P. Oberholzer, P. Boillat, Local Characterization of PEFCs by differential cells: systematic variations of current and asymmetric relative humidity, J. Electrochem. Soc. 161 (1) (2013) 139–152.

[11] L. Hao, P. Cheng, Lattice boltzmann simulations of water transport in gas diffusion layer of a polymer electrolyte membrane fuel cell, J. Power Sources 195 (12) (2010) 3870–3881.

[12] P.K. Sinha, C.Y. Wang, Pore-network modeling of liquid water transport in gas diffusion layer of a polymer electrolyte fuel cell, Electrochim. Acta 52 (28) (2007) 7936–7945.

[13] P.K. Sinha, P.P. Mukherjee, C.Y. Wang, Impact of GDL structure and wettability on water management in polymer electrolyte fuel cells, J. Mater. Chem. 17 (30) (2007) 3089–3103.

[14] J. Hinebaugh, Z. Fishman, A. Bazylak, Unstructured pore network modeling with heterogeneous PEMFC GDL porosity distributions, J. Electrochem. Soc. 157 (11) (2010) 1651–1657.

[15] M. Fazeli, J. Hinebaugh, A. Bazylak, Investigating inlet condition effects on PEMFC GDL liquid water transport through pore network modelling, J. Electrochem. Soc. 162 (7) (2015) 661–668.

[16] J.T. Gostick, Random pore network modeling of fibrous PEMFC gas diffusion media using Voronoi and Delaunay tessellations, J. Electrochem. Soc. 160 (8) (2013) 731–743.

[17] R. Wu, X. Zhu, Q. Liao, H. Wang, Y.D. Ding, J. Li, D.D. Ye, A pore network study on water distribution in bi-layer gas diffusion media: effects of inlet boundary condition and micro-porous layer properties, Int. J. Hydrogen Energy 35 (17) (2010) 9134–9143.

[18] R. Wu, X. Zhu, Q. Liao, H. Wang, Y.D. Ding, J. Li, D.D. Ye, A pore network study on the role of micro-porous layer in control of liquid water distribution in gas diffusion layer, Int. J. Hydrogen Energy 35 (14) (2010) 7588–7593.

[19] Y. Ji, G. Luo, C.Y. Wang, Pore-level liquid water transport through composite diffusion media of pemfc, J. Electrochem. Soc. 157 (12) (2010) 1753–1761.

[20] C. Qin, Water transport in the gas diffusion layer of a polymer electrolyte fuel cell: dynamic pore-network modeling, J. Electrochem. Soc. 162 (2015) 1036–F1046.

[21] K.J. Lee, J.H. Nam, C.J. Kim, Pore-network analysis of two-phase water transport in gas diffusion layers of polymer electrolyte membrane fuel cells, Electrochem. Acta 54 (2009) 1166–1176.

[22] K.J. Lee, J.H. Kang, J.H. Nam, C.J. Kim, Steady liquid water saturation distribution in hydrophobic gas-diffusion layers with engineered pore paths: an invasion-percolation pore-network analysis, J. Power Sources 195 (11) (2010) 3508–3512.

[23] K.J. Lee, J.H. Kang, J.H. Nam, Liquid water distribution in hydrophobic gas diffusion layers with interconnect rib geometry: an invasion-percolation pore network analysis, Int. J. Hydrogen Energy 39 (2014) 6646–6656.

[24] E.F. Medici, J.S. Allen, Evaporation, two phase flow, and thermal transport in porous media with application to low-temperature fuel cells, Int. J. Heat Mass Transf. 65 (2013) 779–788.

[25] B. Straubhaar, J. Pauchet, M. Prat, Water transport in gas diffusion layer of a polymer electrolyte fuel cell in the presence of a temperature gradient. Phase change effect, Int. J. Hydrogen Energy 40 (2015) 11668–11675.

[26] B. Straubhaar, J. Pauchet, M. Prat, Pore network modelling of condensation in gas diffusion layers of proton exchange membrane fuel cells, Int. J. Heat Mass Transf. 102 (2016) 891–901.

[27] N. Belgacem, M. Prat, J. Pauchet, Coupled continuum and condensation-evaporation pore network model of the cathode in polymer-electrolyte fuel cell, Int. J. Hydrogen Energy 42 (12) (2017) 8150–8165.

[28] M. Aghighi, J. Gostick, Pore network modeling of phase change in PEM fuel cell fibrous cathode, J. Appl. Electrochem. (2017), https://doi.org/10.1007/s10800-017-1126-6.

[29] C.Z. Qin, S.M. Hassanizadeh, L.M. Van Oosterhout, Pore-network modeling of water and vapor transport in the micro porous layer and gas diffusion layer of a polymer electrolyte fuel cell, Computation 4 (2) (2016).

[30] A.Z. Weber, R.L. Borup, R.M. Darling, P.K. Das, T.J. Dursch, W. Gu, D. Harvey, A. Kusoglu, S. Litster, M.M. Mench, R. Mukundan, J.P. Owejan, J.G. Pharoah, M. Secanell, I.V. Zenyuk, A critical review of modeling transport phenomena in polymer-electrolyte fuel cells, J. Electrochem. Soc. 161 (2014) 1254–1299.

[31] M. Rebai, M. Prat, Scale effect and two-phase flow in a thin hydrophobic porous layer. Application to water transport in gas diffusion layers of PEM fuel cells, J. Power Sources 192 (2009) 534–543.

[32] H. Tavangarrad, B. Mohebbi, S.M. Hassanizadeh, R. Rosati, J. Claussen, B. Blümich, Continuum-scale modeling of liquid redistribution in a stack of thin hydrophilic fibrous layers, Transp. Porous Media 122 (1) (2018) 203–219.

[33] R. Alink, D. Gerteisen, Modeling the liquid water transport in the gas diffusion layer for polymer electrolyte membrane fuel cells using a water path network, Energies 6 (9) (2013) 4508–4530.

[34] L. Holzer, O. Pecho, J. Schumacher, P. Marmet, O. Stenzel, F.N. Büchi, A. Lamibrac, B. Münch, Microstructure-property relationships in a gas diffusion layer (GDL) for Polymer Electrolyte Fuel Cells, Part I: effect of compression and anisotropy of dry GDL, Electrochim. Acta 227 (2017) 419–434.

[35] A. Lamibrac, J. Roth, M. Toulec, F. Marone, M. Stampanoni, F.N. Büchi, Characterization of liquid water saturation in gas diffusion layers by X-ray tomographic microscopy, J. Electrochem. Soc. 163 (2016) 202–209.

[36] I.V. Zenyuk, D.Y. Parkinson, L.G. Connolly, A.Z. Weber, Gas-diffusion-layer structural properties under compression via X-ray tomography, J. Power Sources 328 (2016) 364–376.

[37] M. Bosomoiu, G. Tsotridis, T. Bednarek, Study of effective transport properties of fresh and aged gas diffusion layers, J. Power Sources 285 (2015) 568–579.

[38] J.T. Gostick, M.A. Ioannidis, M.W. Fowler, M.D. Pritzker, Pore network modelling of fibrous gas diffusion layers for polymer electrolyte membrane fuel cells, J. Power Sources 173 (2007) 277–290.

[39] O.S. Burheim, J.G. Pharoah, H. Lampert, P.J.S. Vie, S. Kjelstrup, Through-plane thermal conductivity of PEMFC porous transport layers, J. Fuel Cell Sci. Technol. 8 (2) (2011).

[40] D. Wilkinson, J.F. Willemsen, Invasion percolation: a new form of percolation theory, J. Phys. A: Math. Gen. 16 (1983) 3365–3376.

[41] P. Deevanhxay, T. Sasabe, S. Tsushima, S. Hirai, Effect of liquid water distribution in gas diffusion media with and without microporous layer on PEM fuel cell performance, Electrochem. Commun. 34 (2013) 239–241.

[42] J.P. Owejan, J.E. Owejan, W. Gu, T.A. Trabold, T.W. Tighe, M.F. Mathias, Water transport mechanisms in PEMFC gas diffusion layers, J. Electrochem. Soc. 157 (2010) 1456–1464.

[43] L. Ceballos, M. Prat, P. Duru, Slow invasion of a non-wetting fluid from multiple inlet sources in a thin porous layer, Phys. Rev. E 84 (2011) 056311.

[44] N. Belgacem, J. Pauchet, M. Prat, On the current distribution at the channel–rib scale in polymer-electrolyte fuel cells, Int. J. Hydrogen Energy 43 (10) (2018) 5112–5123.